# Indo-Pacific Walker circulation drove Pleistocene African aridification

H.J.L. van der Lubbe[a,b,*], I.R. Hall[a,**], S. Barker[a], S. R. Hemming[c], T.F. Baars[d], A. Starr[a], J. Just[e], B.C. Backeberg[f,g,h] and J.C.A. Joordens[i,j,k]

a. School of Earth and Environmental Sciences, Cardiff University, UK
b. Department of Earth Sciences, Faculty of Science, Vrije Universiteit (VU), Amsterdam, the Netherlands
c. Earth and Environmental Sciences, Lamont-Doherty Earth Observatory, USA
d. Department of Geosciences and Engineering, Delft University of Technology, TU Delft, the Netherlands
e. Department of Geosciences, Universität Bremen, Germany
f. Deltares, Delft, the Netherlands
g. Nansen Environmental and Remote Sensing Center, Bergen, Norway
h. Nansen-Tutu Centre for Marine Environmental Research, Cape Town, South Africa
i. Naturalis Biodiversity Center, Leiden, the Netherlands
j. Faculty of Science and Engineering, Maastricht University, the Netherlands
k. Faculty of Archaeology, Leiden University, the Netherlands

Keywords: Pacific Walker Cell, Indian Ocean, Mozambique Channel, IODP Site U1476, eastern African hydroclimate, hominin evolution

*. H.J.L.vander.Lubbe@vu.nl

**Hall@cardiff.ac.uk

## Abstract

Today, the eastern African hydroclimate is tightly linked to fluctuations in the zonal atmospheric Walker circulation[1,2]. A growing body of evidence indicates that this circulation shaped hydroclimatic conditions in the Indian Ocean region also on much longer, glacial-interglacial timescales[3,4,5], following the development of Pacific Walker circulation at ~2.2-2.0 million years ago (Ma)[6,7]. However, continuous long-term records elucidating the timing and mechanisms of Pacific-influenced climate transitions in the Indian Ocean have been unavailable. Here, we present a ~7-million-year-long record of wind-driven circulation of the tropical Indian Ocean, as recorded in Mozambique Channel Throughflow (MCT) flow speed variations. We show that the MCT flow speed was relatively weak and steady until 2.1 ± 0.1 Ma, when it began to increase coincident with intensification of Pacific Walker circulation[6,7]. Strong increases during glacials, reaching maxima after the Mid-Pleistocene Transition (0.9-0.64 Ma[8]), were punctuated by weak flow speeds during interglacials. We provide a mechanism explaining that increasing MCT flow speeds reflect synchronous development of the Indo-Pacific Walker cells that promotes aridification in Africa. Our results suggest that after ~2.1 Ma, the increasing aridification is punctuated by pronounced humid interglacial periods. This record will facilitate testing of hypotheses of climate-environmental drivers for hominin evolution and dispersal.

## Introduction

The upper ocean circulation in the Indian Ocean (IO) is driven by the negative wind stress curl induced by the confluence of SE trade winds and equatorial surface flow of the Walker circulation (Extended Data Fig. 1). Associated strong ocean-atmosphere interactions occur in upwelling zones of the southeastern tropical IO off Sumatra, the equatorial western IO (including Seychelles–Chagos Thermocline Ridge; SCTR[9]), and the Arabian Sea. The coupled ocean-atmosphere zonal circulation drives fluctuations in the eastern African rainfall[1,10]. The predominantly dry air-masses that descend over the cool western IO cause (semi-)arid conditions in eastern Africa[11], while occasional reversals in the Walker circulation, cause floods at interannual timescales[1]. It has been suggested that Walker circulation variability shaped eastern African rainfall also over much longer timescales (>10-100 ka), thereby potentially influencing hominin evolution and dispersal[3,4,12,13]. However, long-term, continuous and well-dated high-resolution proxy records capturing this system have been unavailable to explore the influence of the invigorating Walker circulation on the IO region. Here, we present a detailed flow speed record of Mozambique Channel Throughflow (MCT) off the eastern African coast that constitutes the western limb of the tropical IO gyre system (Fig. 1). This MCT flow speed record is based on lithogenic properties of sediments in a marine core retrieved from International Ocean Discovery Program (IODP) Site U1476 (15°49.25′S; 41°46.12′E, 2166 m water depth)[14] at the Davie Ridge, a bathymetric high in the narrows of the Mozambique Channel (Fig. 1; Methods; Extended Data Figure 5c).

**Mozambique Channel Throughflow**

Annually, the upper ocean circulation of the MCT routes large amounts (~17 Sv [1 Sv = $10^6 m^3 \cdot s^{-1}$]) of IO water southwards into the Agulhas Current[15] (Figure 1a). The MCT is dominated by the regular southward propagation of ~300-350 km wide deep-reaching anti-cyclonic eddies, which affect the near-bottom currents[15]. An enhanced MCT is coupled to the variability in the year-round combined westward flow of the South Equatorial Current (SEC) and its extension, the North-eastern Madagascar Current (NEMC), north of Madagascar[16], which bifurcates upon approaching the African coast into the Eastern African Coastal Current (EACC) and the southward MCT (Fig. 1a).

In the east, the Indonesian Throughflow (ITF) supplies water-masses from the western Pacific Ocean, which directly feed into the southward Leeuwin Current along western Australia, and are additionally advected by the SEC[17]. To the west, the SEC is modulated by the wind-driven tropical and subtropical gyres, and splits east of Madagascar at ~17.5°S into the NEMC and Southeastern Madagascar Current (SEMC) (Fig. 1a). The gyre circulation is driven by the confluence of the south-easterly trade winds (peaking at ~17°S) and the monsoons[18] (Extended data Fig. 1b). To the north, the basin-wide negative wind stress curl induces the divergence of the cyclonic tropical gyre and Ekman pumping, which sustains low dynamic sea surface heights (SSH) at 5°S–12°S, 45°E–90°E (i.e. SCTR)[9], whereas in contrast high SSH occur to the south (Extended Data Fig. 1c). The corresponding meridional SSH gradient forces the climatological westward geostrophic flow of the SEC (Extended Data Fig. 2a-b).

At interannual timescales, the SSH gradient corresponds to anomalies in the coupled atmospheric Indo-Pacific Walker Cell circulation during both negative El Niño–Southern Oscillation (ENSO) and Indian Ocean dipole (IOD) phases[10,19] (Extended Data Figs. 2, 3). During negative phases, the transport of the westward SEC increases and subsequently also that of its extensions: EACC, SEMC, NEMC and most importantly the MCT, and vice versa[20,21,22,23]. At longer timescales, the SSH anomalies in the SEC flow path correspond to the Interdecadal Pacific Oscillation[24], which is very similar to the Pacific Decadal Oscillation and decadal component of ENSO[25]. During 2000-2010, a period characterized by a series of long-lasting La Niña events, the SEC was notably stronger and wider[17]. Coincidently, during recent decades the enhancement of the westward flowing SEC is associated with an increased mean MCT transport, represented by faster southward propagating eddies[18]. Therefore, the MCT is also expected to be sensitive to changes in the Indo-Pacific Walker circulation over longer timescales (Extended Data Fig. 3). Finally, the corresponding intensified upper ocean circulation in the western IO coincides with increased aridity in eastern Africa (Extended Data Figure 4), which can be largely attributed to enhanced upwelling at the SCTR suppressing atmospheric convection[10,17,24].

**MCT flow speed record**

Modern oceanographic observations indicate that the near-bottom currents in the region of Site U1476 (east of the Davie Ridge) typically reflect a weak (on average 0.4-2.8 $cm \cdot s^{-1}$) southerly flow, which is directly below the influence of the energetic eddy-induced currents strongly affecting the upper ~1500 m (Fig. 1c; Extended Data Fig. 5). The region is further sheltered from the northward flowing Mozambique Undercurrent (~1-3 Sv; 3.5-4.5 $cm \cdot s^{-1}$), which is confined to the African continental slope between ~1500-2500 m water depth[15], and it is also disconnected from down-slope sediment transport off the continental margins (Fig. 1b).

Sediment deposition at Site U1476 is current-controlled, as indicated by the strong correlation between abundance of the ‘sortable silt’ fraction (lithogenic sediment between 10-63 μm; SS%) and the sortable silt mean grain size ($\overline{SS}$), which are well within the calibration range for near-bottom current universal flow speed reconstructions (Extended Data Fig. 5; Methods). We therefore argue that the $\overline{SS}$-based reconstructed flow speed variations represent relative changes in MCT flow speed. The age model (Extended Data Fig. 6; Methods) is well-constrained by oxygen isotope ratios ($\delta^{18}O$) recorded in benthic foraminifera over the last 2 Ma and biostratigraphy of calcareous nannofossils over the entire interval, corroborating that the continuous spliced record extends over the past ~7 Ma, at an average resolution of ~5 ka per sediment sample.

The $\overline{SS}$ record shows an average grainsize of 22.6 μm (between 21 to 25 μm), demonstrating relatively stable moderate near-bottom MCT flow speeds, from ~7 Ma until ~2.1 Ma $\pm$ 0.1 Ma (1SD), after which $\overline{SS}$ increases until 0.8 $\pm$ 0.1 Ma (1SD). These statistically significant change-points (Methods) denote a long-term flow speed increase within both glacial and interglacial periods, however the substantial enhancement of MCT flow speed during glacial intervals means that glacial-interglacial variability also increased (>5 cm $s^{-1}$; $\overline{SS}$ range between 23 to 29 μm with a mean of 25.3 μm; Fig 2d). Notable peaks in flow speed are recorded after 2.1 Ma during intense glacial periods (Fig. 3). The long-term increase in MCT flow speed after 2.1 $\pm$ 0.1 Ma is coherent with the accompanying elemental composition and depositional history of sediments at Site U1476 (Extended Data Figs. 6 and 7).

## Climate transitions

Over the last ~7 Ma, several major tectonic and climate transitions occurred that could potentially affect the strength of MCT (Fig. 2). Notably, the Antarctica-to-equator SST gradient steepened during the extensive Late Miocene Cooling (LMC) between 7-5.4 Ma[26]. As a consequence, the southern hemisphere westerlies strengthened and/or migrated northward over the IO causing wetter conditions in Australia[27]. However, the LMC has a similar magnitude in the upwelling zones in the Arabian Sea and equatorial eastern Pacific Ocean (cold tongue), suggesting a minor influence on the zonal atmosphere-ocean circulation in the tropics[26,28], which is consistent with the weak MCT flow speeds during this interval (Fig. 2c).

During the warm Pliocene (5.3-2.6 Ma), both meridional and zonal SST gradients were generally weak[26,28,29]. After the restriction of the Central American Seaway at ~4.3 Ma, the Pacific cold tongue developed first gradually and then at a faster pace during the intensification of Northern Hemisphere Glaciation (NHG; 3.1-2.5 Ma[30])[28]. Synchronously, the meridional SST gradient between eastern equatorial Pacific and northern hemisphere mid-latitudes started at ~4 Ma[31]. Model simulations reveal that the zonal SST increase was twice that of the mid-latitudinal meridional gradient in the Pacific Ocean after ~4 Ma and, notably, was linked to the intensification of the Walker rather than Hadley circulation[32]. After 4-3 Ma, the tectonic constriction of the ITF commenced, progressively reducing the inflow of relatively warm water from the southern Pacific Ocean[33,34]. At ~3.3 Ma, proxy records document considerable cooling of the subsurface eastern IO as well as the surface Leeuwin Current[35,36], which receives direct inflow form the ITF. The latter is linked to the onset of the long-term aridification in western Australia between 3.3-2.4 Ma[37].

Although thermocline shoaling and/or cooling in the path of the SEC (ODP Site 214) is associated with the constriction in ITF, the zonal SST gradient remained weak between the southeastern IO (ODP Site 214) and the (equatorial) western IO (ODP Site 709C)[35] and Arabian Sea (ODP 722)[26]. This suggests that the advection of water-masses from the ITF via the SEC toward the Mozambique Channel and Arabian Sea[17] was limited, with minor effect on MCT flow speed. In agreement, the weak surface wind circulation between 5.0–2.2 Ma[29] is consistent with the relatively stable and sluggish MCT during this interval (Fig. 2). During the intensifying NHG, the net flow of the ITF became further reduced especially during glacials[34]. In contrast, the strongest MCT flow speeds are recorded during glacial periods, in particular after ~0.4 Ma when the Sahul and Sunda shelves became sub-aerially exposed. This indicates that the MCT strength is decoupled from ITF variability and largely unresponsive to both tectonic- and glacially-induced changes in the ITF geometry, in agreement with model simulations indicating that the western boundary transport of the tropical and subtropical gyres remains largely in place without ITF[38]. During a glacially-reduced ITF, the SEC is likely compensated by an increased contribution from intermediate water from the subtropical gyre[39] and probable Tasman leakage. Together, this supports our interpretation that the sensitivity of MCT flow speed is dominantly related to the large-scale coupled atmosphere-ocean circulation in the western IO.

## Intensification of Indo-Pacific Walker Cell

The two statistically significant change points in the long-term MCT coincide with the onset of the Pacific Walker cell intensification (2.2-2.0 Ma)[6] and the MPT (0.9-0.64 Ma)[8], respectively (Methods and Fig. 2b). The initial strengthening of the MCT therefore occurred when the major periodicity (i.e. 41 kyr) and amplitude of glacial-interglacial global ice volume cycles remained relatively constant between 2.5-1.0 Ma. Moreover, this MCT transition occurred well after the intensified NHG (Fig. 2)[40,41]. Despite uncertainties regarding the absolute SST differences between the western Pacific warm pool (ODP Site 806) and the cold tongue that depend on which core locations and proxy types are considered, their long-term (averaging glacial-interglacial variability) divergences robustly indicate that the zonal SST gradient in the equatorial Pacific Ocean reached modern threshold values after 2.2-2.0 Ma[6,42,43]. The development of the Pacific Walker circulation toward its modern mean-state is associated with the expansion of the cold tongue and strengthening of the meridional SST gradient during the enhanced NHG[28]. Thereafter, the strengthened zonal (W-E) SST gradient along the equatorial Pacific Ocean, amplified by the Bjerknes feedback, reflects modern climatology in which easterly surface winds feed into the ascending branch of the Walker cell over the western Pacific Ocean[44] (Extended Data Fig. 8). These large-scale shifts in convection also alter the Indian Walker circulation, which is characterized by westerly winds that ascend over the eastern IO and the Maritime Continent in SE Asia. We therefore infer that the increasing MCT flow speeds after ~2.1 Ma demonstrate the synchronous development of the Indo-Pacific Walker cells.

The SST record of the western Pacific Ocean warm pool (ODP Site 806)[43] beneath the ascending branch of the Pacific Walker cell largely overlaps with those of DSDP Site 214, ODP Site 709C and 722[26,35,36] denoting that temperature gradients were considerably reduced across the IO between 5.0-2.2 Ma (Extended Data Figure 8a). The similarity between the SST records of ODP Site 806 and 709C, both situated within the present-day Indo-Pacific warm pool (IPWP >28˚C), further supports that SST remained high in the eastern IO warm pool after 2.2 Ma. In contrast, after 2.2 Ma SST minima in the Arabian Sea (ODP Site 722) began decreasing to <25.5˚C with long-term mean SST below 28˚C (Fig. 2e). As a consequence, these lower SST suppressed deep atmospheric convection offshore eastern Africa, while strengthening the zonal SST gradient to the IPWP, particularly during glacial periods[26]. The lower glacial SSTs in the Arabian Sea are not directly related to upwelling caused by the SW monsoon[45], but are rather linked to coupled atmospheric-oceanic interactions throughout the tropics[46]. Indeed, the SST difference between the high-resolution records of the IPWP (ODP Site 806) and the Arabian Sea (ODP Site 722) matches well with the inferred increase of the MCT flow (Fig. 3), supporting our interpretation that the invigoration of the coupled zonal atmospheric-oceanic circulation in the IO was synchronized to that of the Pacific Ocean.

## East African Aridification

After 2.1 Ma, the long-term enhancement of Walker circulation would have suppressed (convective) rainfall in eastern Africa, which is likely amplified by decreased SST due to the shoaling of the SCTR, caused by strengthening of tropical gyre. This aridification is documented in the $\delta^{13}C$ record of soil carbonates showing a marked transition from woodlands to grasslands consistent with faunal evidence indicating progressively drier conditions and more open landscapes (Fig. 3e)[47]. This pronounced drying coincides with the long-term significant shift at 1.9 $\pm$ 0.4 Ma towards higher lithogenic sediment accumulation rates in the Arabian Sea[5], which reflect the increasing influence of dust supplied from the Arabian Peninsula and north-eastern Africa by the monsoon as a function source area aridity[12]. The increasing aridification of east Africa significantly postdates that of Australia, which, conversely, is under the direct influence of the ITF[37].

The glacial-interglacial variability that is superimposed on the long-term trend in our MCT record denotes systematically increased MCT during glacial compared to interglacial periods. Our interpretation of an intensified glacial (weaker interglacial) Walker and tropical oceanic gyre circulation is consistent with proxy records that indicate a shallower glacial (deeper interglacial) thermocline at SCTR[48] and off Tanzania[39] during MIS 2, while the opposite occurred in the upwelling zone off Sumatra in the eastern IO[49]. Our MCT flow speed record provides compelling evidence for a systematic intensification of zonal atmospheric and tropical oceanic circulation during glacials, which would cause progressively drier terrestrial conditions in eastern Africa after ~2.1 Ma. Notably, aridity proxies based on soil carbonates and dust are biased toward recording low rainfall amounts, thus dominantly registering arid periods. In contrast, the MCT record sensitively documents flow conditions during both glacial and interglacial periods, suggesting that the well-known long-term aridification trend was punctuated by relatively humid interglacials characterized by weak zonal SST gradients (Fig. 3).

The development towards the modern Walker circulation has been postulated as a significant climate transition influencing hominin evolution in Africa[4]. Our MCT flow speed record appears to be relatively insensitive to major climate changes related to LMC, ITF and NHG (Fig. 3), but closely records the establishment and variability of the Indo-Pacific Walker circulation from 2.1 ± 0.1 Ma onwards. Importantly, the influence of the Indo-Pacific Walker circulation would have extended well beyond eastern Africa. This was recently been shown for the last 0.6 Ma, in the context of early human populations in western and southern Africa[3]. We therefore expect that the results of our study, applied in appropriate theoretical frameworks of environmental drivers for evolution[50], will contribute to increased understanding of humankind's evolutionary path during the Pleistocene.

**References (main text plus figures)**

1. Saji N, Goswami B, Vinayachandran P, Yamagata T. A dipole mode in the tropical Indian Ocean. Nature 1999, 401(6751): 360-363.

2. Tierney JE, Smerdon JE, Anchukaitis KJ, Seager R. Multidecadal variability in East African hydroclimate controlled by the Indian Ocean. Nature 2013, 493(7432): 389-392.

3. Kaboth-Bahr S, Gosling WD, Vogelsang R, Bahr A, Scerri EML, Asrat A, et al. Paleo-ENSO influence on African environments and early modern humans. PNAS 2021, 118(23): 1-6.

4. Maslin MA, Brierley CM, Milner AM, Shultz S, Trauth MH, Wilson KE. East African climate pulses and early human evolution. Quaternary Science Reviews 2014, 101: 1-17.

5. Trauth MH, Larrasoana JC, Mudelsee M. Trends, rhythms and events in Plio-Pleistocene African climate. Quaternary Science Reviews 2009, 28(5-6): 399-411.

6. Etourneau J, Schneider R, Blanz T, Martinez P. Intensification of the Walker and Hadley atmospheric circulations during the Pliocene–Pleistocene climate transition. Earth and Planetary Science Letters 2010, 297(1-2): 103-110.

7. Ravelo AC, Andreasen DH, Lyle M, Olivarez Lyle A, Wara MW. Regional climate shifts caused by gradual global cooling in the Pliocene epoch. Nature 2004, 429(6989): 263-267.

8. Mudelsee M, Schulz M. The Mid-Pleistocene climate transition: onset of 100 ka cycle lags ice volume build-up by 280 ka. Earth and Planetary Science Letters 1997, 151(1-2): 117-123.

9. Hermes J, Reason C. Annual cycle of the South Indian Ocean (Seychelles-Chagos) thermocline ridge in a regional ocean model. Journal of Geophysical Research: Oceans 2008, 113(C4): 1-10.

10. Rao SA, Behera SK. Subsurface influence on SST in the tropical Indian Ocean: structure and interannual variability. Dynamics of Atmospheres and Oceans 2005, 39(1): 103-135.

11. Nicholson SE. Climate and climatic variability of rainfall over eastern Africa. Reviews of Geophysics 2017, 55(3): 590-635.

12. deMenocal PB. African climate change and faunal evolution during the Pliocene–Pleistocene. Earth and Planetary Science Letters 2004, 220(1): 3-24.

13. Levin NE. Environment and climate of early human evolution. Annual Review of Earth and Planetary Sciences 2015, 43: 405-429.

14. Hall IR, Hemming SR, LeVay LJ, Barker S, M.A. B, Brentegani L, et al. South African Climates (Agulhas LGM Density Profile). College Station, TX (USA): International Ocean Discovery Program; 2017.

15. Ullgren J, van Aken H, Ridderinkhof H, De Ruijter W. The hydrography of the Mozambique Channel from six years of continuous temperature, salinity, and velocity observations. Deep Sea Research Part I: Oceanographic Research Papers 2012, 69: 36-50.

16. Backeberg BC, Reason CJC. A connection between the South Equatorial Current north of Madagascar and Mozambique Channel Eddies. Geophysical Research Letters 2010, 37(4): 1-6.

17. Makarim S, Sprintall J, Liu Z, Yu W, Santoso A, Yan X-H, et al. Previously unidentified Indonesian Throughflow pathways and freshening in the Indian Ocean during recent decades. Scientific Reports 2019, 9(1): 1-13.

18. Backeberg BC, Penven P, Rouault M. Impact of intensified Indian Ocean winds on mesoscale variability in the Agulhas system. Nature Climate Change 2012, 2(8): 608-612.

19. Paris ML, Subrahmanyam B, Trott CB, Murty VSN. Influence of ENSO Events on the Agulhas Leakage Region. Remote Sensing in Earth Systems Sciences 2018, 1(3): 79-88.

20. Palastanga V, Van Leeuwen P, De Ruijter W. A link between low-frequency mesoscale eddy variability around Madagascar and the large-scale Indian Ocean variability. Journal of Geophysical Research: Oceans 2006, 111(C9): 1-15.

21. Ridderinkhof H, van der Werf PM, Ullgren JE, van Aken HM, van Leeuwen PJ, de Ruijter WPM. Seasonal and interannual variability in the Mozambique Channel from moored current observations. Journal of Geophysical Research: Oceans 2010, 115(C6): 1-18.

22. Ridderinkhof W, Le Bars D, Von der Heydt A, De Ruijter W. Dipoles of the south east Madagascar current. Geophysical Research Letters 2013, 40(3): 558-562.

23. Yamagami Y, Tozuka T. Interannual variability of South Equatorial Current bifurcation and western boundary currents along the Madagascar coast. Journal of Geophysical Research: Oceans 2015, 120(12): 8551-8570.

24. Jin X, Kwon Y-O, Ummenhofer CC, Seo H, Schwarzkopf FU, Biastoch A, et al. Influences of Pacific climate variability on decadal subsurface ocean heat content variations in the Indian Ocean. Journal of Climate 2018, 31(10): 4157-4174.

25. van Oldenborgh GJ, Doblas-Reyes FJ, Wouters B, Hazeleger W. Decadal prediction skill in a multi-model ensemble. Climate Dynamics 2012, 38(7): 1263-1280.

26. Herbert TD, Lawrence KT, Tzanova A, Peterson LC, Caballero-Gill R, Kelly CS. Late Miocene global cooling and the rise of modern ecosystems. Nature Geoscience 2016, 9: 843–847

27. Groeneveld J, Henderiks J, Renema W, McHugh CM, De Vleeschouwer D, Christensen BA, et al. Australian shelf sediments reveal shifts in Miocene Southern Hemisphere westerlies. Science Advances 2017, 3(5): 1-9.

28. Liu J, Tian J, Liu Z, Herbert TD, Fedorov AV, Lyle M. Eastern equatorial Pacific cold tongue evolution since the late Miocene linked to extratropical climate. Science Advances 2019, 5(4): 1-7.

29. Fedorov A, Brierley C, Lawrence KT, Liu Z, Dekens P, Ravelo A. Patterns and mechanisms of early Pliocene warmth. Nature 2013, 496(7443): 43-49.

30. Haug GH, Tiedemann R, Zahn R, Ravelo AC. Role of Panama uplift on oceanic freshwater balance. Geology 2001, 29(3): 207-210.

31. Brierley CM, Fedorov AV, Liu Z, Herbert TD, Lawrence KT, LaRiviere JP. Greatly Expanded Tropical Warm Pool and Weakened Hadley Circulation in the Early Pliocene. Science 2009, 323(5922): 1714-1718.

32. Tierney JE, Haywood AM, Feng R, Bhattacharya T, Otto-Bliesner BL. Pliocene Warmth Consistent With Greenhouse Gas Forcing. Geophysical Research Letters 2019, 46(15): 9136-9144.

33. Cane MA, Molnar P. Closing of the Indonesian seaway as a precursor to east African aridification around 3–4 million years ago. Nature 2001, 411(6834): 157-162.

34. Petrick B, Martínez-García A, Auer G, Reuning L, Auderset A, Deik H, et al. Glacial Indonesian Throughflow weakening across the Mid-Pleistocene Climatic Transition. Scientific Reports 2019, 9(1): 1-13.

35. Karas C, Nürnberg D, Gupta AK, Tiedemann R, Mohan K, Bickert T. Mid-Pliocene climate change amplified by a switch in Indonesian subsurface throughflow. Nature Geoscience 2009, 2(6): 434-438.

36. Karas C, Nürnberg D, Tiedemann R, Garbe-Schönberg D. Pliocene Indonesian Throughflow and Leeuwin Current dynamics: Implications for Indian Ocean polar heat flux. Paleoceanography 2011, 26(2): 1-9.

37. Christensen BA, Renema W, Henderiks J, De Vleeschouwer D, Groeneveld J, Castañeda IS, et al. Indonesian Throughflow drove Australian climate from humid Pliocene to arid Pleistocene. Geophysical Research Letters 2017, 44(13): 6914-6925.

38. Chen Z, Wu L, Qiu B, Sun S, Jia F. Seasonal variation of the South Equatorial Current bifurcation off Madagascar. Journal of physical oceanography 2014, 44(2): 618-631.

39. Rippert N, Baumann K-H, Pätzold J. Thermocline fluctuations in the western tropical Indian Ocean during the past 35 ka. Journal of Quaternary Science 2015, 30(3): 201-210.

40. Ahn S, Khider D, Lisiecki LE, Lawrence C. A probabilistic Pliocene–Pleistocene stack of benthic δ18O using a profile hidden Markov model. Dynamics and Statistics of the Climate System 2017, 2(1): 1-16.

41. Zachos J, Pagani M, Sloan L, Thomas E, Billups K. Trends, rhythms, and aberrations in global climate 65 Ma to present. Science 2001, 292(5517): 686-693.

42. Ravelo AC, Lawrence KT, Fedorov A, Ford HL. Comment on "A 12-million-year temperature history of the tropical Pacific Ocean". Science 2014, 346(6216): 1467.

43. Wara MW, Ravelo AC, Delaney ML. Permanent El Niño-like conditions during the Pliocene warm period. Science 2005, 309(5735): 758-761.

44. Bjerknes J. Atmospheric teleconnections from the equatorial Pacific. Monthly weather review 1969, 97(3): 163-172.

45. Emeis K-C, Anderson DM, Doose H, Kroon D, Schulz-Bull D. Sea-Surface Temperatures and the History of Monsoon Upwelling in the Northwest Arabian Sea during the Last 500,000 Years. Quaternary Research 1995, 43(3): 355-361.

46. Herbert TD, Peterson LC, Lawrence KT, Liu Z. Tropical ocean temperatures over the past 3.5 million years. Science 2010, 328(5985): 1530-1534.

47. Bobe R, Behrensmeyer AK. The expansion of grassland ecosystems in Africa in relation to mammalian evolution and the origin of the genus Homo. Palaeogeography, Palaeoclimatology, Palaeoecology 2004, 207(3): 399-420.

48. Kiefer T, McCave IN, Elderfield H. Antarctic control on tropical Indian Ocean sea surface temperature and hydrography. Geophysical Research Letters 2006, 33(24): 1-5.

49. Mohtadi M, Prange M, Schefuß E, Jennerjahn TC. Late Holocene slowdown of the Indian Ocean Walker circulation. Nature Communications 2017, 8(1): 1-8.

50. Faith JT, Du A, Behrensmeyer AK, Davies B, Patterson DB, Rowan J, et al. Rethinking the ecological drivers of hominin evolution. Trends in Ecology & Evolution 2021: 797-807.

## Methods

### Sediment core

IODP Expedition 361 Site U1476 Holes A, D and E (15˚49.25′S; 41˚46.12′E, 2166 water depth) yielded a continuous spliced section with a total length of ~242 m. All samples depths are reported against the shipboard spliced CCSF depth scale[14,51]. Site U1476 is situated on the eastern flank of the Davie Ridge at the northern entrance of the Mozambique Channel near the Deep-Sea Drilling Project (DSDP) Site 242. The dominant greenish grey sediments are mainly composed of calcareous nannofossils and foraminifera with low amounts of lithogenic sediments (on average <58 %) and notable occurrences of fine to medium sand[14,51].

### Grain-size analysis

Prior to grain-size analysis, the lithogenic fraction was isolated by the removal of the calcium carbonate and organic matter using HCl (0.5%) and $H_2O_2$ (30%), respectively[52]. No additional removal steps were applied to the sediment, since the amount of biogenic opal is minimal throughout the core[14]. The remaining fractions were routinely scrutinized under a light microscope to confirm the complete removal of biogenic constituents. Grain-size distributions (n=1492) of the remaining lithogenic fraction were analysed using a Sympatec HELOS/KR laser diffraction particle-size analyser at the Laboratory for Sediment Analysis, the Vrije Universiteit Amsterdam (VU, the Netherlands). The sortable silt ($\overline{SS}$; 10-63 μm) geometric mean and percentages were obtained from the laser sizer derived grain-size distributions[53], which cover 57 bins between 0.12 and 2000 μm. The two upper and lower bins were split in order to capture the $\overline{ss}$ range following the approach of McCave et al. (2019)[54].

## XRF Bulk Chemistry

A high-resolution (1 cm) record of qualitative bulk chemistry was acquired from the spliced core of Site U1476 using an Avaatech core scanner at the Scripps Institute of Oceanography. Prior to core scanning, core halves were carefully cleaned and the fresh sediment surface was covered with SPEXCerti Ultralene® to avoid drying out of the sediment surface and contamination of the detector surface. Element intensities (in counts per second; cps) of Ca, Fe and Ti were measured at 10 kV, whereas elements Zr and Rb were obtained at generator settings of 30 kV at Scripps Institute of Oceanography. The natural logs (ln) of relevant elemental ratios are presented because they are reversibly scalable and linearly correlated to the actual elemental concentrations[55].

Importantly, these combined records are consistent with the decreased sediment accumulation rate observed at Site U1476 over the last ~2 Ma (Extended Data Fig. 6), and regionally with the upward-coarsening trends of discontinuous sedimentary sequences in the southern Mozambique Channel[56]. Conversely, if the Site U1476 signals were related to increased deposition of riverine sediments close to the upper slope and to associated down-slope transport after exposure of the continental shelf (mainly <50 m water depth), it would have led to an increase rather than the observed decrease in sediment accumulation under the intensified glacial periods[53].

## Chronology

To reconstruct the age model, benthic isotope data of at least 3 specimens of *Cibicides wuellerstorfi* from the fraction > 350 μm were obtained from the shipboard spliced record that has been derived by stratigraphic linking of cores from Holes A, D and E. The $\delta^{18}O$ measurements (n=626) were performed using a Thermo Finnigan MAT 253 mass spectrometer equipped with a Carbo Kiel carbonate preparation device at the School of Earth and Ocean Sciences, Cardiff University. The long-term precision is better than ± 0.05‰ for the in-house standard (BCT63). All reported $\delta^{18}O$ values are expressed relative to the (Vienna Pee Dee Belemnite) V-PDB scale.

The chronology of spliced core of IODP Site U1476 is based on the correlation of the $\delta^{18}O$ benthic record with the global probabilistic stack (Prob-stack)[40] using 38 tie points for the last ~2 Ma using a comparable approach as[57]. The age-depth relationship agrees with the biochronology of calcareous nannofossils and planktonic foraminifera with only some minor deviations from the $\delta^{18}O$ calibrated record. Below the interval of the benthic isotope stratigraphy spanning last 2 Ma, the chronology of core is constrained by shipboard biostratigraphy of calcareous nannofossils[14,58], which has been further refined by Tangunan et al. (2018)[59]. Deviations of the shipboard biochronology of planktonic foraminifera might be partly attributable to the use of general low latitude calibrations rather than specific ones for the tropical western Indian Ocean[14,51]. Taking into the account the uncertainties on both age and depth constraints, the age-depth-model for the spliced record of IODP Site U1476 was established by the Matlab® application *Undatable*[60] using 10,000 iterations with 30 % of the age-depth constraints randomly removed for bootstrapping and a default xfactor of 0.1. The median age with ±1SD (68.2% percentiles) and ±2SD (95.4% percentiles) are calculated for each centimetre as well as the median sediment accumulation rate (Extended data figure 6).

**Time series analyses**

The change points of the sortable silt record were determined using RAMPFIT[61] and applying search ranges of 1.5-3.5 Ma and 0-2 Ma, using 200 bootstrap iterations. For this study, large, overlapping search windows were used to objectively define change points, while changes in search windows have only a minor effect on the obtained changes points. RAMPFIT estimates the linear change between to changes points, which are defined by the medians of the bootstrap iterations and their standard deviations (1SD). The inferred change points indicate an overall increase in mean sortable silt from 22.6332 ± 0.0595 µm to 25.2640 ± 0.0847 µm between 2.1059 ± 0.1211 Ma and 0.8247 ± 0.1185 Ma, which postdates the intensification of the Northern Hemisphere Glaciation.

The SST of record of ODP 806[43] was downscaled to the temporal resolution of that of ODP 722[26,46,62] using linear interpolation. Hereafter, SST gradient between Indo-Pacific warm pool and upwelling zone of the western Indian Ocean and Arabian Sea was calculated by subtracting of these records and applying a 10-point running mean. After 3.35 Ma, the resolution of the SST record of 722 decreases from ~2 ka to 93 ka rendering its utility to further extend this high-resolution SST gradient record.

Based on[13], time-series of $\delta^{13}$C values from soil carbonate were first determined for Afar region, Omo-Turkana basin, and southern Kenyan-Tanzanian sites, whereby median values are used, in case time-equivalent $\delta^{13}$C determinations are available. These time-series were combined denoting their means, inter-quartile, minimum and maximum ranges using five data-point bins.

**References (Unique to methods)**


51. Hall IR, Hemming SR, LeVay LJ. South African climates (Agulhas LGM Density Profile). 2016.

52. Konert M, Vandenberghe J. Comparison of laser grain size analysis with pipette and sieve analysis: a solution for the underestimation of the clay fraction. Sedimentology 1997, 44(3): 523-535.

53. Van der Lubbe H, Tjallingii R, Prins MA, Brummer G-JA, Jung SJ, Kroon D, et al. Sedimentation patterns off the Zambezi River over the last 20,000 years. Marine Geology 2014, 355: 189-201.

54. McCave I, Andrews J. Distinguishing current effects in sediments delivered to the ocean by ice. I. Principles, methods and examples. Quaternary Science Reviews 2019, 212: 92-107.

55. Weltje GJ, Tjallingii R. Calibration of XRF core scanners for quantitative geochemical logging of sediment cores: theory and application. Earth and Planetary Science Letters 2008, 274(3-4): 423-438.

56. Miramontes E, Penven P, Fierens R, Droz L, Toucanne S, Jorry SJ, et al. The influence of bottom currents on the Zambezi Valley morphology (Mozambique Channel, SW Indian Ocean): In situ current observations and hydrodynamic modelling. Marine Geology 2019, 410: 42-55.

57. Starr A, Hall IR, Barker S, Rackow T, Zhang X, Hemming SR, et al. Antarctic icebergs reorganize ocean circulation during Pleistocene glacials. Nature 2021, 589(7841): 236-241.

58. Anthonissen DE, Ogg JG. Appendix 3 - Cenozoic and Cretaceous Biochronology of Planktonic Foraminifera and Calcareous Nannofossils. In: Gradstein FM, Ogg JG, Schmitz MD, Ogg GM (eds). The Geologic Time Scale. Elsevier: Boston, 2012, pp 1083-1127.

59. Tangunan DN, Baumann K-H, Just J, LeVay LJ, Barker S, Brentegani L, et al. The last 1 million years of the extinct genus Discoaster: Plio–Pleistocene environment and productivity at Site U1476 (Mozambique Channel). Palaeogeography, Palaeoclimatology, Palaeoecology 2018, 505: 187-197.

60. Lougheed BC, Obrochta SP. A Rapid, Deterministic Age-Depth Modeling Routine for Geological Sequences With Inherent Depth Uncertainty. Paleoceanography and Paleoclimatology 2019, 34(1): 122-133.

61. Mudelsee M. Ramp function regression: a tool for quantifying climate transitions. Computers & Geosciences 2000, 26(3): 293-307.

62. Huang Y, Clemens SC, Liu W, Wang Y, Prell WL. Large-scale hydrological change drove the late Miocene C4 plant expansion in the Himalayan foreland and Arabian Peninsula. Geology 2007, 35(6): 531-534.

## Data availability statement

All new benthic oxygen isotopic and lithogenic grain-size data of the spliced record of IODP Site U1476 are available via www.pangaea.de at https://doi.pangaea.de/10.1594/PANGAEA.933831 and https://doi.pangaea.de/10.1594/PANGAEA.933833, respectively.

## Acknowledgements

We are grateful to the government of Mozambique for their permission for deep-sea drilling operations in the context of palaeoclimate and palaeoceanography research. We greatly appreciate to entire shipboard party of IODP Expedition 361 'South African Climates' for their tireless efforts at sea. Furthermore, S. Conn, M. Hagen, S. Lordsmith, A. Nederbragt, L. Owen, M.P. Prins, S.

Rumping, S. Slater, C.W Nooitgedacht, F. van Bakel and C. van Eijbergen are thanked for laboratory assistance. This research used samples and data provided by the Integrated Ocean Drilling Program (IODP). Funding for this work was provided in part by the Dutch Research Council (NWO) Open Programme (grant no. 824.01.005 to H.J.L.v.d.L. and grant no. 016.Vidi.171.049 to J.C.A.J.) and the UK Natural Environment Research Council (grant no. NE/P000037/1 to I.R.H. and NE/P000878/1 to S.B.). We further acknowledge R.D. Norris and N. Mantke for XRF scanning the spliced record of Site U1476.

## Author contributions

IODP Expedition 361 was led by I.R.H. and S.R.H. S.B produced the benthic oxygen isotope record and J.J. the XRF bulk chemistry records. H.J.L.v.d.L. and I.R.H. designed the research, H.J.L.v.d.L performed the grain-size analysis with inputs of T.F.B. and performed further data analyses with inputs from I.R.H. and A.S. H.J.L.v.d.L. conducted oceanographic and climatic analyses with inputs from B.C.B. H.J.L.v.d.L. wrote the manuscript with contributions of I.R.H., J.C.A.J. and A.S. All authors contributed to the data interpretation and commented on the final manuscript. T.F.B. edited the figure layout for publication.

## Competing interests

The authors declare no competing interests

## Figure legends

**Figure 1 | Regional oceanographic settings of IODP Site U1476 (2166 m water depth). a**, *Map of the western Indian Ocean showing major upper-oceanic currents together with bathymetry (General Bathymetric Chart of the Oceans (GEBCO); Extended data figure 1b), eastern African lakes and key hominin sites providing the soil carbonate data (green triangles, Fig 3e)*[13]*. IODP Site U1476 (yellow dot) is under the influence of the Mozambique Channel Throughflow (MCT), which exists largely due to the southward propagation of large anti-cyclonic eddies triggered by the combined westward flow of the South Equatorial Current (SEC) and Northeast Madagascar Current (NEMC) north of Madagascar. The SEC and NEMC form the southern boundary of the cyclonic tropical gyre that further comprises the northward East African Coastal Current (EACC) and South Equatorial Counter Current (SECC). To the south, the Southeast Madagascar Current (SEMC) forming the western boundary of the anti-cyclonic subtropical gyre, induces eddies south* *of Madagascar. These eddies join the Agulhas Current (AC) together with the Mozambique Channel eddies.* ***b,*** *Bathymetry of the Mozambique Channel with the 2.2 km depth contour (thin solid black line) that marks the bathymetric height of the Davie Ridge. Two sections (S1 and S2) are indicated by dashed lines.* ***c****, W-E depth transect across the narrows of Mozambique Channel along S1 and S2 indicating the long-term flow contours (cm $s^{-1}$), whereby negative (positive) values and solid (dashed) contours reflect southward (northward) flow*[15]*. The zero contour along the eastern African margin envelopes the southward flowing Mozambique Undercurrent (MUC)*[15]*.*

**Figure 2 | Climatic and oceanographic over the past 7 million years (from bottom to top).** ***a****, Compilation of global oxygen isotope ratios ($\delta^{18}O$) in benthic foraminifera*[40,41] *with a long-term trend as a 400-kyr running average (yellow).* ***b,*** *Histograms with normal density curves display the MCT change points (Fig. 2c) for 200 bootstrap simulations (Methods).* ***c****, Sortable silt mean ( $\overline{SS}$) flow speed record from IODP Site U1476 (brown), with the black line representing the best fit based on the change points with uncertainty limits (1SD).* ***d,*** *Normalized variance of sortable silt mean ($\overline{SS}$) computed in a 400-kyr running window.* ***e****, The SST proxy records displayed with their 400-kyr running averages with 1SD uncertainty levels of the Indo-Pacific warm pool (IPWP, ODP 806*[43]*, Mg/Ca-based), Arabian Sea (ODP 722*[26]*, $U^{K'}_{37}$ alkenone-based) and upwelling in the eastern tropical Pacific Ocean (ODP 847*[43]*, Mg/Ca-based) mark the onset of the intensification of the atmospheric Walker Cell circulation at ~2.2-2.0 Ma*[6]*. The black dashed line at 28°C denotes the critical threshold for atmospheric deep convection.* ***f****, For illustration, major taxa and events in the hominin evolutionary record*[13]*. Vertical grey bars indicate tectonic and climatic transitions*[6,8,26,30,33]*.*

**Figure 3 | MCT and eastern African aridity records with distinct glacial and interglacial intervals over the past 3.3 Ma (from bottom to top)**. ***a****, Oxygen isotope ratios ($\delta^{18}O$) of benthic foraminifera at IODP Site U1476 (purple) with the global $\delta^{18}O$ benthic probabilistic stack (Prob-stack, black)*[40]*.* ***b****, Marine Isotope Stages (MIS). Purple shaded vertical bars highlight intense glacial intervals, whereas orange ones mark some pronounced interglacial periods.* ***c****, Sortable silt ($\overline{SS}$) flow change speed record from IODP Site U1476 (brown) with SST gradient ($\Delta SST$) between the IPWP (ODP 806 – ODP 214)*[36,43] *and Arabian Sea (ODP 722)*[26]*(green; Methods).* ***d****, The accumulation of northeast African and Arabian aeolian dust in the Arabian Sea (Site 721-722)*[12] *statistically increases at 1.86 $\pm$ 0.44 Ma based on the BREAKFIT with uncertainty limits*

*(SE) (dashed line)*[5]. ***e**, Carbon isotope ratios (*$\delta^{13}C$*) of soil carbonates*[13] *plotted as inter-quartiles boxes with horizontal lines denoting the means and whiskers indicating the minima and maxima using five data-point bins.* ***f**, For illustration, key events in Homo evolution and dispersal*[13].

## Extended data legends

**Extended Data Figure 1 | Coupled oceanographic and atmospheric circulation of the Indian Ocean region a**, Surface circulation indicated by mean geostrophic velocities and directions. IODP Site U1476 is situated in the Mozambique Channel, which experiences a net southward flow of the Mozambique Channel Throughflow (MCT). The tropical Indian gyre receives and redistributes inflow from the Indonesian Throughflow (ITF). The main components of the tropical Indian gyre: East African Coastal Current (EACC), Southern Equatorial Current (SEC), Southern Equatorial Counter Current (SECC) and Northeast Madagascar Current (NEMC) are highlighted with a dark grey outline marking the mean extension of the tropical gyre[63,64]. At ~60˚E, the SEC bifurcates into two main branches feeding into the NEMC and the Southeastern Madagascar Current (SEMC) as it crosses bathymetric highs including the Mascarene Plateau, highlighted by the solid grey bathymetric contour at 2.2 km water depth. The SEMC is outside the outline of the tropical gyre as it is part of the anti-cyclonic subtropical gyre. **b**, Mean wind stress (black arrows) and wind stress curl of the Indian Ocean indicate the basin-wide negative (positive) wind stress curl forcing the tropical (subtropical) gyre. A black line indicates the zero wind stress curl. **c**, Mean dynamic sea surface topography indicating a sea-level low between 10-5˚S at the centre of the tropical Indian gyre; the Seychelles–Chagos thermocline ridge (SCTR)[9]. The thicker contour of 1.05 m denotes the northern extent of the subtropical gyre, whereby the blues (reds) highlight lower (higher) sea surfaces, which are associated with the cyclonic (anti-cyclonic) circulation of the tropical (subtropical) gyres.

The bathymetric, oceanic (1993-2012) and surface wind data (1979-2019) are derived from: General Bathymetric Chart of the Oceans (GEBCO)[65], CNES-CLS18 MDT[66], ERA5 monthly-averaged data on single levels (DOI: 10.24381/cds.6860a573), respectively. These maps are generated with MATLAB® and Mapping Toolbox, version 9.8.0.1323502 (R2020a, Natick, Massachusetts: The MathWorks Inc., United States).

**Extended Data Figure 2 | Dynamic sea surface topography in meters superimposed by the mean of monthly Indian Ocean sea surface height (SSH) maps a**, Composite of all monthly SSH between 1999-2019, superimposed on dynamic sea surface topography, marks sea-level low of the SCTR (5°S–12˚S, 45˚E–90˚E)[9]. Solid red line refers to cross section along longitude 52˚E between latitudes 25 to 5˚S, across the SEC, see b. **b**, Mean dynamic sea surface gradient at 52˚E (red thick line) as marked by solid black line in a, c, d, e and f. Meridional surface height gradient and associated near-surface pressure gradient south of the SCTR drives (influenced by Coriolis force) the westward deep-reaching South Equatorial Current (SEC). Positive (negative) SSH anomalies formed during ENSO and IOD propagate westward as downwelling (upwelling) Rossby waves in ca. 6 months[10,19,24,67]. The dynamic sea surface topography averaged over 6 months following positive Indian Ocean Dipole (+IOD), negative Indian Dipole (-IOD), positive El Niño Southern Oscillation (ENSO) - El Niño, and negative ENSO - La Niña are shown in c, d, e and f, respectively. **g**, IOD and ENSO time series with solid vertical lines indicating long-term mean with ±1SD and ±2SD (dashed lines). Red dots mark the months that are selected after a positive IOD (c) and ENSO (e) events, while blue dots mark the months after negative IOD (d) and ENSO (f) events. SSH anomalies induced by ENSO and IOD often reinforce each other[10], since they are linked at interannual[1] to decadal time-scales[63], at least over the last millennium[68].

Sea surface topography, SSH maps, IOD SST index[1], El Niño 3.4 SST Index[69] are from Ssalto/Duacs-Cnes; https://www.aviso.altimetry.fr, https://psl.noaa.gov/gcos_wgsp/Timeseries/DMI/, https://psl.noaa.gov/gcos_wgsp/Timeseries/Nino34. These maps are generated with MATLAB® and Mapping Toolbox, version 9.8.0.1323502 (R2020a, Natick, Massachusetts: The MathWorks Inc., United States).

**Extended Data Figure 3 | 3d representations of the mean sea surface topography**, averaged over 6 months after (**a**) warm (positive) and (**b**) cold (negative) ENSO-IOD phases, respectively induced by regional anti-cyclonic (AC) positive and cyclonic (C) negative wind stress curls along the equatorial Indian Ocean west of 100˚E, which is coupled to the atmospheric Pacific Walker Cell circulation[10,24]. In contrast, sea surface height (SSH) variability in the eastern Indian Ocean is derived from the western Pacific Ocean via the Indonesian Throughflow (ITF; Extended Data Fig. 1a, 2c-f). Black arrows indicate schematic representation of the zonal Walker circulation. During positive ENSO phases, the center of atmospheric deep convection shifts eastward, resulting in anomalous descending air masses over the western Pacific Ocean and Maritime Continent[63]. The corresponding anomalous easterlies induce down-welling Rossby waves in the central Indian

Ocean that propagate westward as positive SSH anomalies, increasing the thermocline depth at the SCTR while decreasing the meridional SSH gradient and corresponding SEC in the western Indian Ocean[10,24] (Extended Data Figure 2b). Conversely, the SSH gradient and in turn the SEC flow increases during negative ENSO phases. The associated westerlies/easterlies induce upwelling and thermocline shoaling (dark blue) in the western/eastern Indian Ocean, and in turn promote deep atmospheric convection and excess rainfall over the Maritime Continent/eastern Africa via sea atmospheric interactions[10,17]. The Mozambique Channel Throughflow (MCT) that is related to the westward flow of the SEC north of Madagascar therefore decreases following a negative-cold ENSO-IOD phase (b) and vice versa (a).

**Extended Data Figure 4 | Precipitation difference (mm/day) of mean precipitation between 2000-2012 minus that of 1979-1999** indicating systematically drier conditions in eastern Africa during the last decade[17], which coincides with intensified Southern Equatorial Current (SEC)[17] and Mozambique Channel Throughflow (MCT)[70]. Green triangles indicate the eastern African hominin sites (1. Afar Basin, 2. Omo-Turkana Basin, 3. Baringo and Tugen Hills, 4. Kanjera 5. Olorgesailie, 6. Laetoli and Olduvai), from which long-term carbon isotope records of soil carbonates are available serving as long-term proxy of East African aridity. The rainfall data is from Global Precipitation Climatology Project (GPCP) monthly precipitation analysis (1979–present; DOI 10.7289/V56971M6) and visualized with MATLAB® and Mapping Toolbox, version 9.8.0.1323502 (R2020a, Natick, Massachusetts: The MathWorks Inc., United States).

**Extended Data Figure 5 | Flow speed reconstructions using sortable silt mean grain size and abundance in the Mozambique Channel, a**, 3-part diagram of sortable silt properties of flow speed in the Mozambique Channel (Clock-wise). The relationship between sortable silt abundance (% lithogenic fraction between 10-63 μm; SS%) and mean grain size ($\overline{SS}$)[54,71,72] for the spliced record from Site IODP U1476[14] and modern surface sediments (64PE304-47, -51, -56, -63, -66 and -68)[53]. The strong correlation (Pearsons correlation coefficient = 0.79) indicates that sortable silt deposition was subject to current sorting and selective transport[71]. The $\overline{SS}$ of U1476 and nearby surface sediments are well within the calibration range for universal near-bottom current flow speed reconstructions[71]. The inferred flow speeds for the surface sediment samples using the universal $\overline{SS}$ flow speed calibration correspond to the +2SD from the mean near-bottom currents obtained from nearby mooring stations. The flow directions are southwards except for those of the Mozambique undercurrent (MUC) that is confined to the eastern African margin below 1.5 km water depth[15]. The $\overline{SS}$ is likely somewhat biased towards to higher near bottom flow speeds, as the finest fractions that may have selectively deposited during slow near-bottom current conditions were preferentially removed under intra- and interannually increased near-bottom currents. Additionally, slight deviations from the mean flow speed might be further attributed to the regional nature of the lithogenic sediments, as most $\overline{SS}$ flow speed calibrations are defined for the northern Atlantic Ocean[71]. However, the sensitivity is comparable amongst the local calibrations and therefore the inferred relative changes in flow speed are also accurate for the Mozambique Channel, albeit the absolute values may slightly differ. In this study, the coarsest $\overline{SS}$ and in turn highest flow speeds are obtained from near and within the topographic depression, where the continuation of the MUC passes through the Davie Ridge[73]. **b,** W-E transect across the Mozambique Channel with long-term flow contours (cm $s^{-1}$)[15] as in Fig. 1c, but superimposed by the mean flow speeds of individual moorings of mean near-bottom currents across the Mozambique Channel (cm $s^{-1}$)[21,74], whereby negative (positive) values reflect southward (northward) flow. **c,** Mozambique Channel bathymetric map with transect across Site IODP U1476 (S2) and the mooring transect (S1) with station (small solid black squares). The mean near-bottom flow speeds vectors recorded at the mooring transect are indicated by dashed[74] and solid[21] lines. The locations of the surface sediment samples are marked by white dots with black outlines (64PE304-47, -51, -56, -63, -66 and -68)[53].

**Extended Data Figure 6** | Age model of the spliced record of IODP Site U1476. **a**, From top to bottom: The chronology of spliced core of IODP Site U1476 is based on the correlation of the $\delta^{18}$O benthic record with the global $\delta^{18}$O benthic probabilistic stack (Prob-stack)[40] using 38 tie points for the last ~2 Ma. Benthic $\delta^{18}$O record of the spliced record of IODP Site U1476 over the last ~2 Ma (blue) and Prob-stack (black)[40]. Minimal number of tie-points that are used to tune the $\delta^{18}$O benthic record of U1476 to Prob-stack are indicated by vertical lines in **a** following a similar approach as[57]. The Prob-stack overlain by the tuned benthic $\delta^{18}$O record of the spliced record of IODP Site U1476 demonstrates the similarity between both records. **b**, The age-depth relationship agrees with the biochronology of calcareous nannofossils and planktonic foraminifera with only some minor deviations from the $\delta^{18}$O bayesian age model. Bayesian age-modeling[60] of U1476 with $\pm$1SD (dark grey) and $\pm$2SD (light grey) based on the benthic $\delta^{18}$O tuning points and biostratigraphy of calcareous nannofossils over the last 3 Ma with the accumulation rates. The shipboard biostratigraphy of calcareous nannofossils[14], which has been further refined by Tangunan et al.(2018)[59] displaying internal agreement. **c**, Idem as **b** for the last ~7 Ma, Deviations of the shipboard biochronology of planktonic foraminifera might be partly attributable to the use of general low latitude calibrations rather than specific calibrations for the tropical western Indian Ocean[14,51].

**Extended Data Figure 7 | 7-Ma long records of sortable silt mean ($\overline{SS}$) and derived flow speed changes together with lithogenic properties.** The accompanying elemental compositions are obtained through X-ray Fluorescence (XRF) analyses of sediments at Site U1476 (Methods). The glacial periods are indicated for the last 5.3 Ma[75] by vertical light blue bars. The 10-point running means of the lithogenic ln (Zr/Rb) record reflect the relative deposition of dense Zr grains that are sorted, via selective deposition, together with silt-sand sized terrigenous particles, and Rb that is mainly present in clay minerals as substitution for K. Additionally, the 10-point running means of XRF bulk record (ln) Ca/(Fe or Ti) record that represent the relative deposition of carbonates (including foraminiferal shells) versus the terrigenous fraction[53]. Reconstructed enhancements in flow speed after 2.1 $\pm$ 0.1 Ma correspond to increases in coarse-grained lithogenic sediments together with increases in marine carbonates, which suggests selective deposition and removal of the fine-grained lithogenic sediment fractions.

**Extended Data Figure 8 | Long-term Sea Surface Temperature (SST) records and Indo-Pacific Walker Cell circulation. a,** Long-term SST records from the Indian and Pacific Ocean. The Mg/Ca-based SST records of DSDP 214[35], ODP 709C[36], 806 and 847[43] that are calcuated and corrected for dissolution at depth[76] are mainly derived from *Globigerinoides sacculifer,* therefore recording temperatures about 20-30 m below the surface[76]. Divergence of the SST records at ~2.1 Ma reflects the onset of the modern Indo-Pacfiic Walker cell circulation. **b,** Representation of present-day coupled Indo-Pacific Walker cell circulation, which is characterized by climatological low-level westerlies[11] and easterlies over the equatorial Indian and Pacific Oceans, respectively. The corresponding moisture-laden air masses of both oceans ascend over the Maritime Continent in southeastern Asia and the associated atmospheric deep convection induces excess rainfall. In contrast, the subsiding dry air masses over the cool western Indian Ocean cause arid conditions in eastern Africa. **c,** Ocean map color gradients show climatological mean Sea Surface Temperature (SST)[77] and black arrows represent the atmospheric surface circulation of the Indian and Pacific Ocean basins. The low-level Pacific easterlies and Indian westerlies are driven by the temperature contrast between the center of the Indo-Pacific Warm Pool (IPWP; SST >28$^{\circ}$C) and upwelling areas in the eastern Pacific Ocean (Cold tongue) and western Indian Ocean (Seychelles-Chagos Thermocline Ridge (SCTR), western Indian Ocean and Arabian Sea). The yellow dots indicate IODP Site U1476 (this study), and U1337[28], DSDP Site 214[35], ODP Sites 709C[36], 721-722[12,46,62], 806 and 847[43] providing long-term SST records, as well as sites GeoB12610-2[39] and GeoB10038-4[49] that date back to the Last Glacial Maximum (LGM).

The SST map has been derived from NOAA Extended Reconstructed Sea Surface Temperature (ERSST) (Version 5, NOAA National Centers for Environmental Information, DOI:10.7289/V5T72FNM) is plotted with MATLAB® and Mapping Toolbox, version 9.8.0.1323502 (R2020a, Natick, Massachusetts: The MathWorks Inc., United States).

**References (Unique to extended data)**


63. Schott FA, Xie SP, McCreary Jr JP. Indian Ocean circulation and climate variability. Reviews of Geophysics 2009, 47(1): 1-46.

64. McCreary JP, Kundu PK, Molinari RL. A numerical investigation of dynamics, thermodynamics and mixed-layer processes in the Indian Ocean. Progress in Oceanography 1993, 31(3): 181-244.

65. IOC, IHO, BODC. CentenaryEdition of the GEBCO Digital Atlas. 2003.

66. Mulet S, Rio MH, Etienne H, Artana C, Cancet M, Dibarboure G, et al. The new CNES-CLS18 Global Mean Dynamic Topography. Ocean Sci Discuss 2021, 2021: 1-31.

67. Putrasahan D, Kirtman BP, Beal LM. Modulation of SST Interannual Variability in the Agulhas Leakage Region Associated with ENSO. Journal of Climate 2016, 29(19): 7089-7102.

68. Abram NJ, Wright NM, Ellis B, Dixon BC, Wurtzel JB, England MH, et al. Coupling of Indo-Pacific climate variability over the last millennium. Nature 2020, 579(7799): 385-392.

69. Rayner NA, Parker DE, Horton EB, Folland CK, Alexander LV, Rowell DP, et al. Global analyses of sea surface temperature, sea ice, and night marine air temperature since the late nineteenth century. Journal of Geophysical Research: Atmospheres 2003, 108(D14): 1-29.

70. McCave I, Thornalley D, Hall I. Relation of sortable silt grain-size to deep-sea current speeds: Calibration of the 'Mud Current Meter'. Deep Sea Research Part I: Oceanographic Research Papers 2017, 127: 1-12.

71. McCave IN, Manighetti B, Robinson SG. Sortable silt and fine sediment size/composition slicing: parameters for palaeocurrent speed and palaeoceanography. Paleoceanography 1995, 10(3): 593-610.

72. van Aken HM, Ridderinkhof H, de Ruijter WP. North Atlantic deep water in the south-western Indian Ocean. Deep Sea Research Part I: Oceanographic Research Papers 2004, 51(6): 755-776.

73. Ridderinkhof H, De Ruijter W. Moored current observations in the Mozambique Channel. Deep Sea Research Part II: Topical Studies in Oceanography 2003, 50(12-13): 1933-1955.

74. Lisiecki LE, Raymo ME. A Pliocene-Pleistocene stack of 57 globally distributed benthic $\delta^{18}O$ records. Paleoceanography 2005, 20(1): 1-17.

75. Dekens PS, Lea DW, Pak DK, Spero HJ. Core top calibration of Mg/Ca in tropical foraminifera: Refining paleotemperature estimation. Geochemistry, Geophysics, Geosystems 2002, 3(4): 1-29.

76. NESDIS NA. WORLD OCEAN ATLAS 2018. 2019.

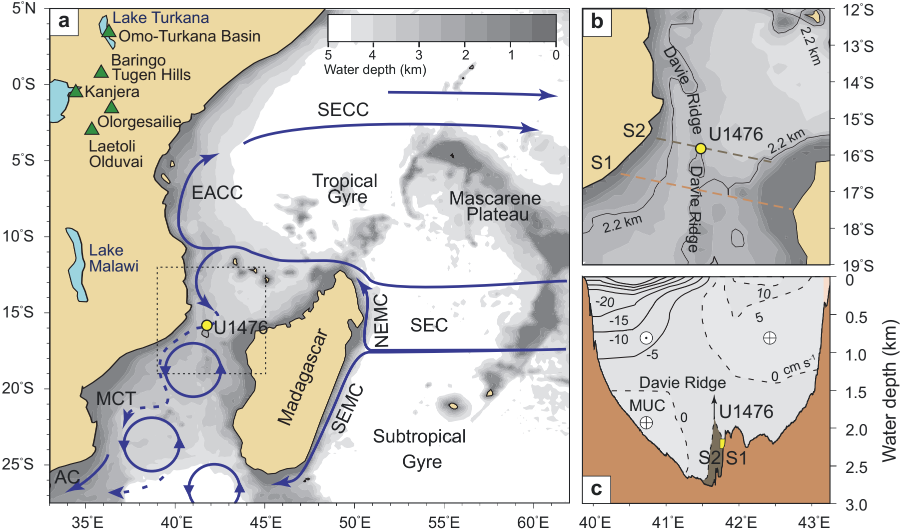

a
Lake Turkana
Omo-Turkana Basin
Baringo
Tugen Hills
Kanjera
Olorgesailie
Laetoli
Olduvai
Lake Malawi
Water depth (km)
5 4 3 2 1 0
SECC
EACC
Tropical Gyre
Mascarene Plateau
U1476
NEMC
SEC
Madagascar
SEMC
Subtropical Gyre
MCT
AC
5˚N
0˚S
5˚S
10˚S
15˚S
20˚S
25˚S
35˚E
40˚E
45˚E
50˚E
55˚E
60˚E
b
Davie Ridge
2.2 km
S2
S1
U1476
12˚S
13˚S
14˚S
15˚S
16˚S
17˚S
18˚S
19˚S
c
-20
-15
-10
-5
10
5
0 cm s-1
Davie Ridge
MUC
0
U1476
S2
S1
Water depth (km)
0
0.5
1.0
1.5
2.0
2.5
3.0
40˚E
41˚E
42˚E
43˚E

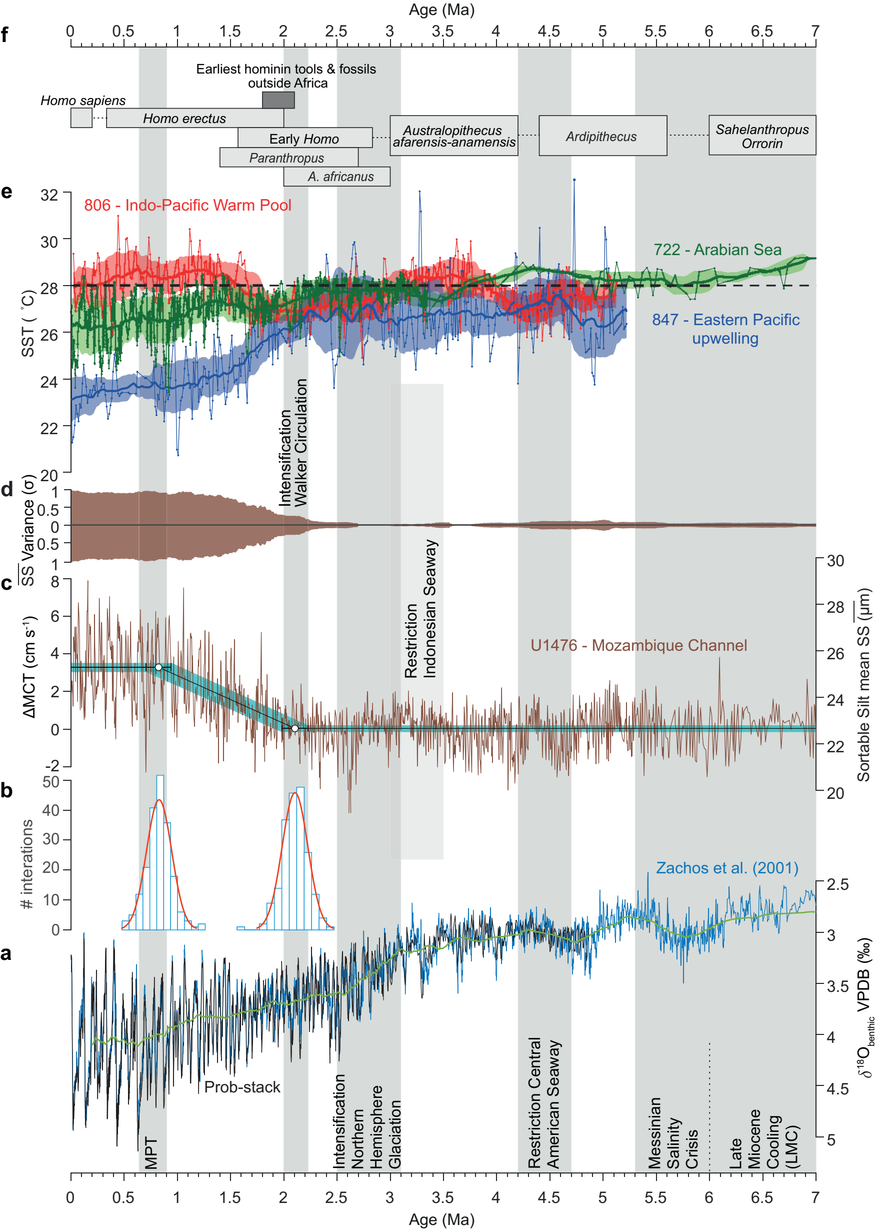

Age (Ma)
f
Earliest hominin tools & fossils outside Africa
Homo sapiens
Homo erectus
Early Homo
Paranthropus
A. africanus
Australopithecus afarensis-anamensis
Ardipithecus
Sahelanthropus Orrorin
e
806 - Indo-Pacific Warm Pool
722 - Arabian Sea
847 - Eastern Pacific upwelling
SST (°C)
Intensification Walker Circulation
d
SS Variance (σ)
Restriction Indonesian Seaway
c
ΔMCT (cm s-1)
U1476 - Mozambique Channel
Sortable Silt mean SS (µm)
b
# interations
Zachos et al. (2001)
a
Prob-stack
δ18O benthic VPDB (‰)
MPT
Intensification Northern Hemisphere Glaciation
Restriction Central American Seaway
Messinian Salinity Crisis
Late Miocene Cooling (LMC)
Age (Ma)

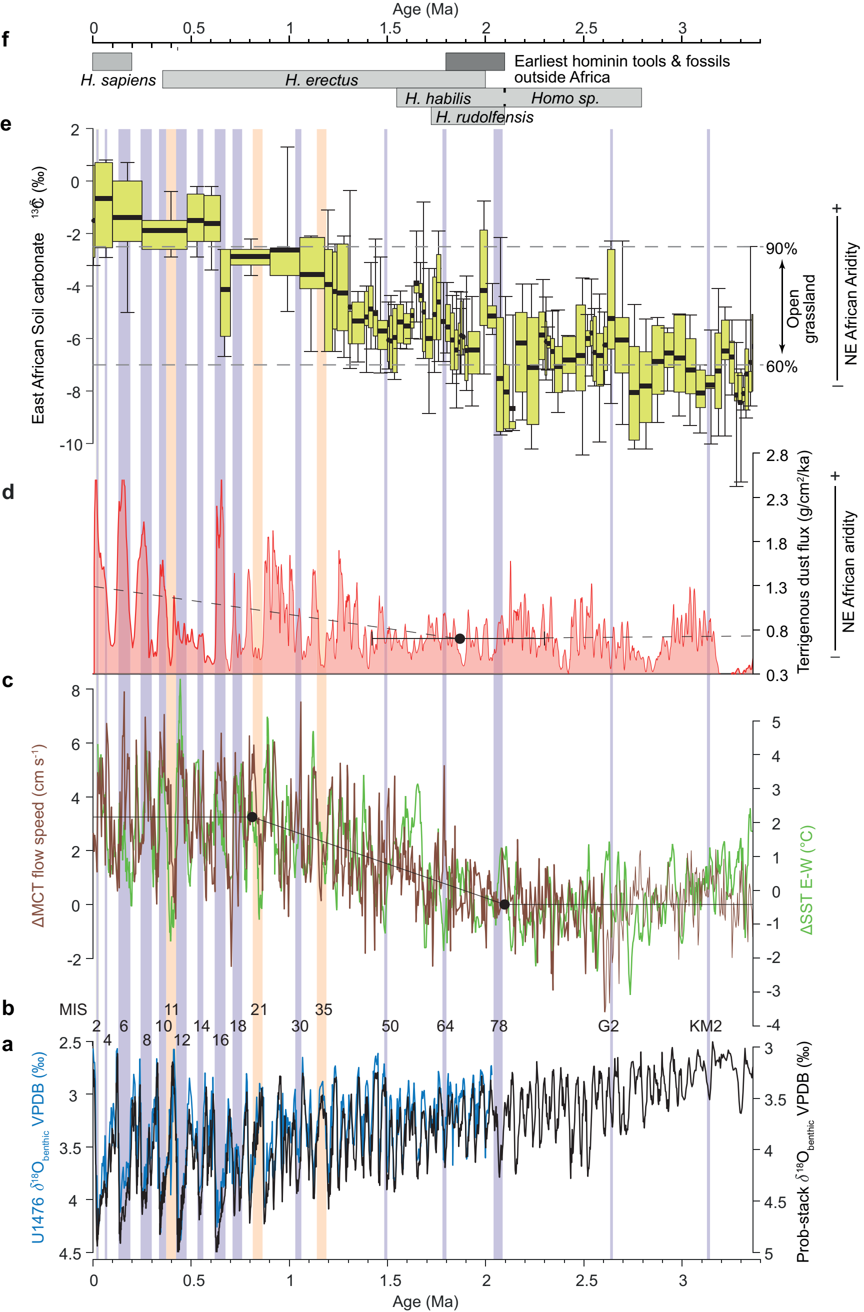

Age (Ma)
f
Earliest hominin tools & fossils outside Africa
H. sapiens
H. erectus
H. habilis
Homo sp.
H. rudolfensis
e
East African Soil carbonate δ13C (‰)
90%
Open grassland
60%
NE African Aridity
d
Terrigenous dust flux (g/cm2/ka)
NE African aridity
c
ΔMCT flow speed (cm s-1)
ΔSST E-W (°C)
b
MIS
2
4
6
8
10
11
12
14
16
18
21
30
35
50
64
78
G2
KM2
a
U1476 δ18Obenthic VPDB (‰)
Prob-stack δ18Obenthic VPDB (‰)
Age (Ma)